J Math Chem (2009) 45:790–818
DOI 10.1007/s10910-008-9462-8

ORIGINAL PAPER

Exact quantification of time signals from magnetic resonance spectroscopy by the fast Padé transform with applications to breast cancer diagnostics

Dževad Belkić · Karen Belkić

Received: 14 August 2008 / Accepted: 2 September 2008 / Published online: 23 September 2008

Abstract Mathematical modeling via the fast Padé transform (FPT) is applied according to experimental NMR data encoded from (a) normal, non-infiltrated breast tissue, (b) benign pathology (fibroadenoma) and (c) malignant breast tissue. At a partial signal length $N_P = 1500$, the FPT provided exact reconstruction of all the input spectral parameters for the time signals corresponding to the normal, benign as well as to the malignant lesions. The converged parametric results remained stable at longer signal lengths. The Padé absorption spectra yielded unequivocal resolution of all the extracted physical metabolites, even of those that were nearly completely overlapping (phosphocholine and phosphoethanolamine at 3.22 ppm). The capacity of the FPT to resolve and precisely quantify the physical resonances as encountered in normal versus benign versus malignant breast is demonstrated. In particular, the FPT unambiguously delineated and quantified diagnostically important metabolites such as lactate, as well as choline, phosphocholine and glycerophosphocholine that are very closely overlapping and may represent MR-retrievable molecular markers of breast cancer. This was achieved by the FPT without any fitting or numerical integration of peak areas. We conclude that these advantages of the FPT could be of definite benefit for breast cancer diagnostics via NMR and that this line of investigation should continue with encoded data from benign and malignant breast tissue, in vitro and in vivo. We anticipate that Padé-optimized MRS will reduce the false positive rates of MR-based modalities and further improve their sensitivity. Once this is achieved, and given that

Dž. Belkić (✉) · K. Belkić
Department of Oncology-Pathology, Karolinska Institute, P.O. Box 260, Stockholm 17176, Sweden
e-mail: Dzevad.Belkic@ki.se

K. Belkić
Institute for Prevention Research, University of Southern California Keck School of Medicine, Los Angeles, CA 91803, USA
e-mail: Karen.Belkic@ki.se

MR entails no ionizing radiation, new possibilities for screening/early detection open up, especially for risk groups, e.g. Padé-optimized MRS could be used with greater surveillance frequency among younger women with high breast cancer risk.

Keywords Breast cancer · Magnetic resonance spectroscopy · Time signals · Quantification · Fast Padé transform

Abbreviations

Ala	Alanine
au	Arbitrary units
β-Glc	Beta-glucose
CDP	Cytosine diphosphate
Cho	Choline
FID	Free induction decay
FFT	Fast Fourier transform
FPT	Fast Padé transform
FWHM	Full width at half maximum
GPC	Glycerophosphocholine
HLSVD	Hankel–Lanczos singular value decomposition
Lac	Lactate
m-Ino	Myoinositol
MR	Magnetic resonance
MRI	Magnetic resonance imaging
MRS	Magnetic resonance spectroscopy
MRSI	Magnetic resonance spectroscopic imaging
NMR	Nuclear magnetic resonance
PA	Padé approximant
ppm	Parts per million
PC	Phosphocholine
PE	Phosphoethanolamine
SNR	Signal-to-noise ratio
SNS	Signal–noise separation
Tau	Taurine
TE	Echo time
TSP	3-(trimethylsilyl-) 3,3,2,2-tetradeutero-propionic acid

1 Introduction

Early cancer detection is nearly always associated with markedly improved prognosis. In order to achieve this survival advantage, resolution enhancement and accurate quantification of encoded biomedical data are critical [1]. Insufficient accuracy of the algorithms that are commercially available and built into clinical scanners hinders progress, especially in diagnostic modalities based upon magnetic resonance spectroscopy (MRS) and spectroscopic imaging (MRSI). Mathematics are of decisive importance for enhancing the information yield of MRS and MRSI [1]. In this paper,

we will focus upon the potential advantages of the fast Padé transform (FPT) applied to MRS as these could specifically impact upon early detection of breast cancer, a disease which affects an estimated 12% of women during their lifetime and which is the leading cause of cancer-related mortality among women, with over 400,000 deaths per year worldwide [2–4].

1.1 Theory: the fast Padé transform

"*Proof of principle*" investigations [5–15] demonstrate that the fast Padé transform, the FPT as it is acronymed, is a powerful, stable parametric processor with robust error analysis, which provides unequivocal quantification of MRS time signals. The FPT is a non-linear *polynomial quotient* P_L/Q_K of the exact finite-rank spectrum (Green function) given by the Maclaurin series with the encoded raw time signal $\{c_n\}$ as the expansion coefficients. Non-linearity of the FPT yields noise suppression. The FPT has been shown to be stable when signal length is systematically augmented at a fixed bandwidth, producing no spikes or other spectral deformations [10,16]. The FPT is a powerful interpolator and extrapolator [10]. Due to extrapolation, which is present in the implicit polynomial inversion via Q_K^{-1} in P_L/Q_K, inference is gained from a non-measurable infinite number of signal points by using only the available finite set $\{c_n\}(0 \leq n \leq N-1, N < \infty)$. The FPT can use the fixed Fourier mesh $2\pi k/T$ $(k = 0, \ldots, N-1)$, but this is not mandatory. In other words, the FPT can be computed at any frequency ω. Resolution in the FPT is not pre-determined by T, which is the total acquisition time. Moreover, due to its parametric estimation and extrapolation capabilities, the FPT has excellent resolving power.

Quantum mechanics determines that the optimal mathematical model for the frequency spectrum of time signals is prescribed to be the ratio of two polynomials, i.e. the FPT. Thus, just as in the time domain where quantum mechanics predicts the form of the time signal as the sum of complex-valued damped exponentials, by virtue to the time-frequency dual representation, the same physics automatically prescribes that the frequency spectrum is given by the Padé quotient of two polynomials. *This is the origin of the unprecedented algorithmic success of the FPT, via its demonstrable, exact reconstructions*, as shown in our Refs. [9,10,12,13,17].

The polynomial quotient P_K/Q_K (diagonal) or P_{K-1}/Q_K (para-diagonal) as a rational function in harmonic variable $z^{-1} = \exp(-i\omega\tau)$, is known in the literature as the Padé approximant (PA) [18,19]. In signal processing, the PA is alternatively called the FPT [18,19] to highlight the possibility of obtaining a shape spectrum from an FID (free induction decay) via a non-parametric estimation as reminiscent of the fast Fourier transform (FFT). The latter type of estimation in the FPT is done by simply evaluating the Padé spectrum P_K/Q_K without ever searching for any of the spectral parameters that are the complex frequencies $\{\omega_k\}$ and amplitudes $\{d_k\}$. The FPT is the only parametric estimator which computes the envelope spectrum without the need to obtain the set $\{\omega_k, d_k\}$ first. This is in sharp contrast to e.g. Hankel–Lanczos singular value decomposition (HLSVD) [20] which computes the envelope spectrum by first estimating the peak parameters $\{\omega_k, d_k\}$.

Most importantly, the FPT can perform parametric reconstructions by rooting the polynomial Q_K whose roots $\{z_k^{-1}\}$ yield $\{\omega_k\}$ and this readily leads to $\{d_k\}$ for each resonance. For example, the para-diagonal FPT treats the exact spectrum, i.e. the mentioned finite-rank Green function $G_N(z^{-1})$, via the *unique* ratio of two polynomials $P_{K-1}(z^{-1})/Q_K(z^{-1})$ at *any frequency* ω:

$$G_N(z^{-1}) = \frac{1}{N}\sum_{n=0}^{N-1} c_n z^{-n}, \tag{1}$$

$$G_N(z^{-1}) \approx \frac{P_{K-1}(z^{-1})}{Q_K(z^{-1})} = \sum_{k=1}^{K} \frac{d_k}{z^{-1}-z_k^{-1}}, \tag{2}$$

$$P_{K-1}(z^{-1}) = \sum_{r=0}^{K-1} p_r z^{-r}, \quad Q_K(z^{-1}) = \sum_{s=0}^{K} q_s z^{-s}, \tag{3}$$

where $z = e^{i\omega\tau}$ and $z_k = e^{i\omega_k\tau}$. The para-diagonal ($L = K-1$) and diagonal ($L = K$) PA are most frequently used from the set of the general PA, P_L/Q_K, because they incur minimal error in practice. In the FPT, the sum $\sum_{k=1}^{K} d_k/(z^{-1} - z_k^{-1})$ represents the complex-valued *total shape spectrum* (envelope) which is the sum of the K corresponding *component spectra*, $d_k/(z^{-1}-z_k^{-1})(1 \le k \le K)$. Here, P_{K-1} and Q_K are readily extracted from the input data G_N by treating the product $G_N Q_K$ in the defining relation $G_N * Q_K = P_{K-1}$ as the standard convolution [5,10,18].

Crucially, unique to the FPT is its unparalleled capability to unequivocally identify and separate noise from the genuine/physical content of the signal by using the powerful concept of Froissart doublets (pole-zero cancellations) [12–14,21]. As in Ref. [13], a given reconstructed resonance can be identified as true versus spurious by computing a sequence of the Padé shape spectra $\{P_m/Q_m\}$ ($m = 1, 2, 3, \ldots$) in the frequency range of interest. Here, the fingerprint of detection of the exact number K of resonances is the attainment of the stabilization value $m = m'$ after which a saturation is systematically maintained by observing that $P_{m'+q}/Q_{m'+q} = P_{m'}/Q_{m'}$ ($q = 1, 2, 3, \ldots$). This critical transition ($m = m'$) yields the sought K via $K = m'$, as verified to work in practice with MRS signals [13]. This is the concept of Froissart doublets, or equivalently, pole-zero cancellations [12,13,21]. The computation is carried out by gradually and systematically increasing the degree of the Padé polynomials. As these degrees change, the reconstructed spectra fluctuate until stabilization occurs. The value of the polynomial degree at which the predetermined level of accuracy is achieved represents the sought exact number of resonances K. This constancy of the reconstructed values can be obtained, e.g. via the cannonical representation of the Padé polynomial quotients (±: inside/outside the unit circle):

$$\frac{P_{K-1}^{\pm}(z^{\pm 1})}{Q_K^{\pm}(z^{\pm 1})} = \frac{p_{K-1}^{\pm}}{q_K^{\pm}} \frac{\prod_{k=1}^{K-1}(z^{\pm 1} - z_k^{\pm})}{\prod_{k'=1}^{K}(z^{\pm 1} - z_{k'}^{\pm})}, \tag{4}$$

where $\tilde{z}_k^{\pm}$ and $z_k^{\pm}$ are the zeros of polynomials $P_{K-1}^{\pm}$ and $Q_K^{\pm}$, respectively. The quotient form from Eq. 4 leads to cancellation of all the terms in the Padé numerator and denominator polynomials, when the computation is continued after the stabilized value of the order in the FPT has been attained, so that:

$$\frac{P_{K-1+m}^{\pm}(z^{\pm 1})}{Q_{K+m}^{\pm}(z^{\pm 1})} = \frac{P_{K-1}^{\pm}(z^{\pm 1})}{Q_K^{\pm}(z^{\pm 1})} \quad (m = 1, 2, 3, \ldots). \tag{5}$$

The Cauchy residue of $P_{K-1}^{\pm}/Q_K^{\pm}$ from Eq. 5 represents the amplitudes $d_k^{\pm}$ whose analytical expressions are:

$$d_k^{\pm} = \frac{p_{K-1}^{\pm}}{q_K^{\pm}} \frac{\prod_{k'=1}^{K-1}(z_k^{\pm 1} - \tilde{z}_{k'}^{\pm})}{\prod_{k'=1, k' \neq k}^{K}(z_k^{\pm 1} - z_{k'}^{\pm})}. \tag{6}$$

Therefore, it is obvious from Eq. 7 that whenever $z_k^{\pm} = \tilde{z}_k^{\pm}$, the amplitudes $d_k^{\pm}$ of the poles from the Froissart doublets are exactly zero:

$$d_k^{\pm} = 0 \quad \text{for} \quad z_k^{\pm} = \tilde{z}_k^{\pm}. \tag{7}$$

The number of spurious resonances is always several times greater than that of the true metabolites. It is obviously an essential precondition for trustworthy clinical applications that the genuine information be clearly and unambiguously identified. Complete separation of noise from the genuine metabolic information, i.e. signal-noise separation (SNS) has been achieved via the pole-zero cancellations with the FPT. For free induction decays that were noiseless, the FPT returns all the spectral parameters (irrespective of their number) within machine accuracy [13,14,17]. For noise-corrupted FIDs, all the known physical/genuine spectral parameters are retrieved by the FPT within at least 3–4 decimal places for signal to noise ratios (SNR) of the level of those typically encountered in time signals encoded via MRS [13,15].

The clear, direct and immediate importance of these findings has been assessed with respect to clinical oncology. Besides confirming the high resolution and stability of the FPT in general studies of MR total shape spectra, this superior resolution performance of the FPT has also been confirmed with respect to data directly derived from malignant and benign ovarian samples [22,23]. Not only did the FPT markedly enhance resolution of MR spectra compared to the conventional Fourier analysis, but it also yielded the unequivocal, exact parametric data needed to reconstruct the metabolite concentrations which characterize ovarian cancer and distinguish this from non-malignant lesions. These features of the FPT were deemed to be of critical benefit to ovarian cancer diagnostics via MRS, in particular for early detection, a goal which has thus far been elusive, but achievement of which would clearly confer a major survival advantage. We will now briefly describe the current status of breast cancer screening diagnostics focusing upon MR-based modalities, with a view to potential improvements that could be provided by Padé-optimized MRS.

1.2 The current status of breast cancer screening diagnostics with a focus upon MR-based modalities

Systematic early detection through screening with mammography followed by appropriate diagnosis and management have been clearly demonstrated to reduce mortality from breast cancer [24–28]. Mammography has been the mainstay of breast cancer screening. Calcifications due to cancer are depicted thereby, including at the earliest stage: *ductal carcinoma in situ*. However, mammography has relatively poor specificity. For dense breasts seen particularly among young women, its sensitivity is also low (30–48%).

Magnetic resonance-based modalities can aid in early breast cancer detection without exposing the breast, a radiosensitive tissue, to ionizing radiation. This is particularly important in view of (a) the heightened radiosensitivity for women with genetic risk for breast cancer, i.e. with *BRCA* germline mutations, Li Fraumeni syndrome (p53 tumor suppressor gene mutations), as well as those who are heterozygous for ataxia-telangiectasia and (b) that screening for women at high risk should begin at a younger age and with increased frequency [29–31].

Contrast-enhanced magnetic resonance imaging (MRI) is usually very sensitive; there is consistent evidence that MRI is more sensitive than mammography for detecting breast cancer among women with an increased risk [24,32]. Invasive breast cancers that can spread to the lymph nodes and cause distant metastases are frequently non-calcified and therefore they can be very difficult to detect mammographically, especially when the breast parenchyma is dense. It is precisely among the younger women that breast cancer when it does occur, is often biologically more aggressive [27]. The prognostic profiles of breast cancers detected by MRI appear to be relatively favorable, e.g. a higher percentage of node-negative malignancies compared to those detected by other screening methods [33]. The American Cancer Society now recommends MRI for women with an estimated lifetime breast cancer risk at or above 20–25% [24]. Schrading and Kuhl [31] have proposed discontinuing systematic mammographic screening in young women with BRCA1 mutations and instead to use MRI for screening, in light of the vulnerability to ionizing radiation together with the fact that in their series, none of the BRCA-1-associated breast cancers were calcified.

False negative findings have, however, been reported for MRI. This occurs mainly for small tumors, especially if they do not selectively take up contrast. Moreover, MRI cannot reveal microcalcifications [34] and occasionally invasive ductal and lobular carcinomas are missed, although in most studies non-detection with MRI is more common with in situ ductal carcinoma [32,35]. Schrading and Kuhl [31] also note that high-grade tumors among women with BRCA1 mutations often appear similar to "fibroadenoma-like" benign tumors. Recent data suggest that MRI may be more effective for detecting breast cancers among women at high family risk compared to those with low family risk [36].

However, with respect to breast cancer diagnostics, the main problem with MRI is, that despite excellent spatial resolution and generally superior sensitivity, its specificity has been lower than mammography in most series published to date [24,33]. This results in higher call-back and biopsy rates, with approximately 20–40% of these biopsies showing cancer (positive predictive value) [24]. Common benign breast lesions

such as fibroadenomas can sometimes be difficult to distinguish from breast cancer on MRI [37]. Thus, while women at high risk for breast cancer undergoing intensive surveillance programs appear to be relieved by the greater sensitivity of MRI [38], a large number of false positive findings may impact unfavorably upon quality of life [39,40].

By providing insight into the metabolic characteristics of malignancy, MRS can complement the morphological information provided by MRI. In vivo MRS has been shown to increase the specificity of MRI with respect to the diagnosis of breast cancer [41–47]. Thus far, data on over 100 malignant and 100 benign breast lesions have been published. These studies have been based upon the composite choline signal, assessed either qualitatively or quantitatively.

However, with the conventional Fourier-based analysis, in vivo MRS has had limitations related to resolution, SNR as well as being based upon estimates of a single composite compound (total choline). Particularly troublesome is the limited possibility of MRS to characterize smaller tumors, e.g. breast cancers <2 cm, that are difficult to distinguish from benign lesions [44,48–51]. As pointed out by surgical oncologist Gluch [52]: "difficulties arise not so much in regards to the large lesion with suspicious imaging characteristics, but rather the lesion <1 cm in size, or ductal carcinoma in-situ. *In-vivo* studies have not satisfactorily addressed these entities. A chance of missing a breast cancer of the order of only 1% would translate into a significant medicolegal concern." Most importantly, it should be pointed out that a missed cancer, albeit relatively less likely with MRI plus MRS than mammography, can adversely affect prognosis [24].

The reliance upon the composite choline peak for breast cancer detection through MRS may compromise diagnostic accuracy, since choline may also be observed in benign breast lesions. Heretofore, for example, using in vivo MRS a total of 46 fibroadenomas have been evaluated [47] with three false positive findings. Choline also appears in normal breast during lactation, although in the latter, a lactose resonance at 3.8 is typically also seen [51]. It should, however, also be pointed out that breast cancer can coexist with lactation as well as with pregnancy, and these malignancies are often detected late. Furthermore, choline is often undetected in small tumors that are then misclassified as benign [41].

Using Fourier-based analysis, in vivo proton MRS for breast cancer diagnostics has generally required lipid suppression, since the MR spectra from the breast are usually dominated by lipid resonances. This lipid hampers localized shimming and also produces sideband artefacts [50]. Lipid suppression has most often been achieved by increasing the echo time. However, this leads to diminished signal intensity. Very recently, Hu et al. [49] presented some initial data about the possibility of lipid suppression at short echo times via an echo-filter suppression. On the other hand, Stanwell and Mountford [50] point out that suppression of the lipid resonance eliminates the possibility of evaluating lipid which is part of the actual disease process. Overall, use of various echo times impedes consistent interpretation of data from in vivo MRS of the breast [50], and this may have clinically important implications. For example, metabolites with short T_2 relaxation times will have decayed at longer TE; of these is myoinositol whose estimated concentrations provided some useful distinction between breast cancer and fibroadenoma in our analysis [40,53,54] of in vitro MRS data [55].

The high resolution of in vitro nuclear magnetic resonance (NMR) applied to extracted specimens can provide a greater insight into the metabolic activity of cancerous breast tissue. We have performed extensive multivariate analyses [40,53,54] of such NMR data from extracted breast specimens [55] revealing rich spectroscopic information for detecting breast cancer in closely overlapping resonances. Several metabolites (notably lactate) improved diagnostic accuracy, while total choline had somewhat lower diagnostic accuracy compared to several other metabolites, including its closely overlapping components. These findings justify further exploration of how MRS could tap into this rich store of metabolic information. In order to do so, improved data processing methods are needed to quantify MR-visible compounds in breast lesions, as has been recently emphasized [40,53,54,56,57].

1.3 Aim of the present study

In the present study we examine the performance of the FPT applied to time signals that were generated according to in vitro MRS data as encoded from extracted breast specimens [55]. This is viewed as the first step in the process of determining whether the described features of the FPT could be of potential benefit for breast cancer diagnostics via MRS.

2 Results

2.1 Input data

Three FIDs of the following type were generated:

$$c_n = \sum_{k=1}^{K} d_k e^{in\omega_k \tau}, \quad \mathrm{Im}(\omega_k) > 0. \tag{8}$$

via a sum of $K = 9$ damped complex exponentials $\exp(in\tau\omega_k)(1 \le k \le 9)$ with time-independent (stationary) complex amplitudes d_k. Here, ω_k and d_k are the fundamental angular frequencies and amplitudes, ($\omega_k = 2\pi f_k$, with f_k being the linear frequency) and $\mathrm{Re}(z)$ and $\mathrm{Im}(z)$, respectively, denote the real and imaginary parts of a complex number z. The time signals were subsequently quantified using the FPT, as described in [12]. The FIDs from Ref. [55] were recorded at a Larmor frequency of 600 MHz (static magnetic field strength $B_0 \approx 14.1$T). We used a bandwidth of 6 kHz (the inverse of this bandwidth is the sampling time τ) and set the total signal length $N = 2048$.

For the normal (non-infiltrated) breast, the input data for the spectral parameters were according to the median concentrations C_k (expressed in μM/g/ww) (where ww denotes wet weight) from the data of Gribbestad et al. [55] from 12 patients. The input data for a benign breast lesion was according to the concentrations of the nine metabolites from a single fibroadenoma as reported in Ref. [55]. For breast cancer,

the input data for the spectral parameters were from median concentrations from the data of Ref. [55] for 14 samples[1] taken from 12 patients.

The resonances are grouped into two bands: 1.3–1.5 ppm and 3.2–3.3 ppm. Within the latter band, there are seven metabolites, including two that are nearly degenerate around 3.22 ppm. These are phosphocholine (PC) peak #4 and phosphoethanolamine (PE) peak #5 separated by only 2.03×10^{-4} ppm.

We computed the input peak amplitudes d_k from the reported concentrations where $|d_k| = (\mathrm{C_{met}}/\mathrm{C_{ref}}) \times 2$, where $\mathrm{C_{ref}} = 0.05$ mM/g/ww. TSP (3-(trimethylsilyl-) 3,3,2,2-tetradeutero-propionic acid) was used as the internal reference by Gribbestad et al. [55], such that $|d_k| = \mathrm{C_{met}}/[25\mu\mathrm{M/g/ww}]$. The T_2 relaxation times were not reported in Ref. [55]. We took the line widths (full-widths at half-maximum (FWHM)) to be approximately 1 Hz, allowing very small variations, and assuming Lorentzian peaks. The line widths are proportional to Im (f_k). Note that the mentioned smallest chemical shift difference of $\approx 2 \times 10^{-4}$ ppm is 4 times less than the typical line width of 8×10^{-4} ppm. The phases $\varphi_k (1 \leq k \leq 9)$ from complex-valued d_k were all set to zero, so that every d_k becomes real, $d_k = |d_k|$.

The input data for the normal breast tissue (upper panel (i)), fibroadenoma (middle panel (ii)) and for the malignant breast (bottom panel (iii)) are presented in Table 1.

2.2 Reconstructed data

We used the diagonal FPT$^{(-)}$ to analyze the FIDs. The coefficients $\{p_r, q_s\}$ of the polynomials P_K and Q_K were computed by solving the systems of linear equations, treating the product in $G_N(z^{-1}) * Q_K(z^{-1}) = P_K(z^{-1})$ as a convolution. To extract the peak parameters, we solved the characteristic equation $Q_K(z^{-1}) = 0$. This leads to K unique roots $z_k^{-1} (1 \leq k \leq K)$, so that the sought ω_k is deduced via $\omega_k = (i/\tau) \ln(z_k^{-1})$. The FPT extracts the parameters $\{\omega_k, d_k\}$ $(1 \leq k \leq K)$ of every physical resonance directly from the raw encoded FID. The k^{th} metabolite concentration is computed from the reconstructed amplitudes d_k as $\mathrm{C_{met}} = d_k \times (25\,\mu\mathrm{M/g/ww})$.

To establish the constancy of the spectral parameters for all three signals, we systematically increased the signal length for the same bandwidth (i.e. augmenting the acquisition times). Examining the spectral parameters at total orders $K = 500$, 750 and 1,000, where $2K = N_P$ and N_P denotes partial signal length, we found that convergence occurred at $K = 750$ for all three FIDs under study, and remained stable thereafter. We determined whether a given reconstructed resonance was true or spurious by computing a sequence of the Padé shape spectra $\{P_m/Q_m\}$ $(m = 1, 2, 3, \ldots)$ in the frequency range of interest from 1.3–3.3 ppm, as described in Sect. 1.1, Eqs. 4 through 7 and in Ref. [13]. For all three examined FIDs, of the 750 total resonances, 741 were identified as spurious by their zero amplitudes and the pole-zero coincidences, yielding the nine genuine resonances.

[1] Two samples each were taken from two of patients. In Ref. [54] metabolite concentrations were calculated in only six and nine malignant samples, respectively, for the metabolites β-glucose and myoinositol.

Table 1 Input spectral parameters and metabolite concentrations for normal breast tissue (top panel (i)), fibroadenoma (middle panel (ii)) and malignant breast (bottom panel (iii)) derived from in vitro data of Ref. [55]. Hereafter, ppm denotes parts per million, au arbitrary units, ww wet weight, M_k denotes metabolite assignment, C_k denotes concentration of M_k, while Lac denotes lactate, Ala alanine, Cho choline, PC phosphocholine, PE phosphoethanolamine, GPC glycerophosphocholine, β-Glc beta-glucose, Tau taurine, m-Ino myoinositol

INPUT DATA: SPECTRAL PARAMETERS, CONCENTRATIONS and METABOLITE ASSIGNMENTS
Types of Tissue on Three Panels : (i) Normal, (ii) Fibroadenoma, (iii) Malignant

(i) NORMAL

N_k (Metabolite # k)	Re(f_k) (ppm)	Im(f_k) (ppm)	$\lvert d_k \rvert$ (au)	C_k (μM/g/ww)	M_k (Assignment)
1	1.330413	0.000834	0.02016	0.5040	Lac
2	1.470313	0.000832	0.00350	0.0875	Ala
3	3.210124	0.000831	0.00068	0.0170	Cho
4	3.220012	0.000833	0.00076	0.0190	PC
5	3.220215	0.000834	0.00516	0.1290	PE
6	3.230412	0.000832	0.00128	0.0320	GPC
7	3.250224	0.000833	0.01800	0.4500	β–Glc
8	3.270141	0.000831	0.00530	0.1325	Tau
9	3.280132	0.000832	0.01144	0.2860	m–Ino

(ii) FIBROADENOMA

N_k (Metabolite # k)	Re(f_k) (ppm)	Im(f_k) (ppm)	$\lvert d_k \rvert$ (au)	C_k (μM/g/ww)	M_k (Assignment)
1	1.330413	0.000832	0.05928	1.4820	Lac
2	1.470313	0.000834	0.00440	0.1100	Ala
3	3.210124	0.000833	0.00088	0.0220	Cho
4	3.220012	0.000832	0.00432	0.1080	PC
5	3.220215	0.000831	0.01476	0.3690	PE
6	3.230412	0.000833	0.00276	0.0690	GPC
7	3.250224	0.000832	0.03912	0.9780	β–Glc
8	3.270141	0.000834	0.01352	0.3380	Tau
9	3.280132	0.000831	0.01860	0.4650	m–Ino

(iii) MALIGNANT

N_k (Metabolite # k)	Re(f_k) (ppm)	Im(f_k) (ppm)	$\lvert d_k \rvert$ (au)	C_k (μM/g/ww)	M_k (Assignment)
1	1.330413	0.000831	0.32474	8.1185	Lac
2	1.470313	0.000832	0.03156	0.7890	Ala
3	3.210124	0.000834	0.00446	0.1115	Cho
4	3.220012	0.000831	0.02448	0.6120	PC
5	3.220215	0.000832	0.07776	1.9440	PE
6	3.230412	0.000833	0.00936	0.2340	GPC
7	3.250224	0.000832	0.02882	0.7205	β–Glc
8	3.270141	0.000831	0.11182	2.7955	Tau
9	3.280132	0.000833	0.03564	0.8910	m–Ino

2.2.1 Reconstruction of the data from normal breast

The reconstructed data by the FPT$^{(-)}$ for the normal breast tissue are presented in Table 2. These data are shown for partial signal lengths: $N_P = 1000$, $N_P = 1500$ and $N_P = 2000$.

At the shortest signal length, $N_P = 1000$ (upper panel (i)), only eight of the nine resonances were identified. In the interval where there should be two peaks, PC (#4) at 3.220012 ppm and PE (#5) at 3.220215, only one resonance was identified at 3.220189 ppm. Since this single peak was closer to PE, it was given that assignment. At that signal length, the reconstructed amplitudes and, consequently, the concentrations for that single resonance were approximately the sum of (PC + PE). At $N_P = 1000$ all the reconstructed spectral parameters were completely exact for lactate (Lac, peak #1) at 1.330413 ppm, alanine (Ala, peak #2) at 1.470313 ppm, β-glucose (β-Glc, peak #7) at 3.250224 ppm, taurine (Tau, peak #8) at 3.270141 and myoinositol (m-Ino, peak #9) at 3.280132 ppm. While the reconstructed amplitude $|d_k|$ and metabolite concentration were completely correct for choline (Cho, peak #3), the chemical shift frequency, Re(f_k) and the line width, Im(f_k) for choline were correct for five of the six decimal places (3.210123 ppm rather than 3.210124 ppm, 0.000830 ppm rather than 0.000831 ppm, respectively). At $N_P = 1000$ for glycerophosphocholine (GPC, peak #6) the line width, Im(f_k) was correct for five of the six digits (0.000831 ppm rather than 0.000832 ppm), while the reconstructed Re(f_k), $|d_k|$ and concentration were all fully exact to the 4$^{\text{th}}$ decimal place. At $N_P = 1500$ full convergence was attained for all the reconstructed parameters for all nine resonances (middle panel (ii) of Table 2). The stability of convergence at higher signal length $N_P = 2000$ is demonstrated on the bottom panel (iii) of Table 2, in which it is seen that all the reconstructed parameters remain exact. This remains true at still higher N_P including the full signal length N.

Figure 1 shows the absorption component shape spectra and the total shape spectra reconstructed by the FPT$^{(-)}$ at the three partial signal lengths: $N_P = 1000$, $N_P = 1500$ and $N_P = 2000$ for the normal breast data. At $N_P = 1000$, as seen on the right upper panel (iv), the absorption total shape spectrum is converged. This was not the case, however, for the component shape spectrum (left upper panel (i)), which shows only one peak (#5, PE) at 3.22 which is overestimated, while peak #4 (PC) is unresolved. At $N_P = 1500$ in the left middle panel (ii) of Fig. 1 the component shape spectrum is converged such that peaks ## 4 and 5 are resolved and have the correct heights, as do all the other peaks. The small PC peak is seen to completely underlie PE. This is to be expected since, as noted, the difference between these peaks ## 4 and 5 is about four times less than the line widths. Stability of convergence is confirmed at $N_P = 2000$ in the lower panels for both the absorption component shape spectrum (iii) and the total shape spectrum (vi), and at still higher N_P including the full signal length N.

The convergence of metabolite concentrations for the normal breast cancer data is graphically illustrated in Fig. 2 for the same three partial signal lengths: $N_P = 1000$, $N_P = 1500$ and $N_P = 2000$. The input data are represented by the symbol "x", whereas the Padé-reconstructed data are shown as open circles. Prior to convergence, at $N_P = 1000$ neither the concentrations of PC nor PE are correctly assessed in the reconstruction (top panel (i)), but all the rest of the metabolite concentrations are exact to the 4th decimal place. At $N_P = 1500$ (middle panel (ii)) and $N_P = 2000$ (bottom

Table 2 Padé-reconstructed spectral parameters and metabolite concentrations for normal breast tissue with the input data as derived from Ref.[55]

CONVERGENCE of SPECTRAL PARAMETERS and CONCENTRATIONS in FPT$^{(-)}$: PARTIAL SIGNAL LENGTHS N_P =1000, 1500, 2000

(i) Pade–Reconstructed Data (Normal): N_P = 1000 (# 4 PC: Unresolved, # 5 PE: Overestimated)

N_k (Metabolite # k)	Re(f_k) (ppm)	Im(f_k) (ppm)	$\|d_k\|$ (au)	C_k(μM/g/ww)	M_k (Assignment)
1	1.330413	0.000834	0.02016	0.5040	Lac
2	1.470313	0.000832	0.00350	0.0875	Ala
3	3.210123	0.000830	0.00068	0.0170	Cho
5	3.220189	0.000836	0.00592	0.1480	PE
6	3.230412	0.000831	0.00128	0.0320	GPC
7	3.250224	0.000833	0.01800	0.4500	β–Glc
8	3.270141	0.000831	0.00530	0.1325	Tau
9	3.280132	0.000832	0.01144	0.2860	m–Ino

(ii) Pade–Reconstructed Data (Normal): N_P = 1500 (Converged)

N_k (Metabolite # k)	Re(f_k) (ppm)	Im(f_k) (ppm)	$\|d_k\|$ (au)	C_k(μM/g/ww)	M_k (Assignment)
1	1.330413	0.000834	0.02016	0.5040	Lac
2	1.470313	0.000832	0.00350	0.0875	Ala
3	3.210124	0.000831	0.00068	0.0170	Cho
4	3.220012	0.000833	0.00076	0.0190	PC
5	3.220215	0.000834	0.00516	0.1290	PE
6	3.230412	0.000832	0.00128	0.0320	GPC
7	3.250224	0.000833	0.01800	0.4500	β–Glc
8	3.270141	0.000831	0.00530	0.1325	Tau
9	3.280132	0.000832	0.01144	0.2860	m–Ino

(iii) Pade–Reconstructed Data (Normal): N_P = 2000 (Converged)

N_k (Metabolite # k)	Re(f_k) (ppm)	Im(f_k) (ppm)	$\|d_k\|$ (au)	C_k(μM/g/ww)	M_k (Assignment)
1	1.330413	0.000834	0.02016	0.5040	Lac
2	1.470313	0.000832	0.00350	0.0875	Ala
3	3.210124	0.000831	0.00068	0.0170	Cho
4	3.220012	0.000833	0.00076	0.0190	PC
5	3.220215	0.000834	0.00516	0.1290	PE
6	3.230412	0.000832	0.00128	0.0320	GPC
7	3.250224	0.000833	0.01800	0.4500	β–Glc
8	3.270141	0.000831	0.00530	0.1325	Tau
9	3.280132	0.000832	0.01144	0.2860	m–Ino

panel (iii)), all of the metabolite concentrations are correct, as seen both numerically and by the graphic representations. This means that the "x's" are completely centered within the open circles, indicating full agreement between the input and reconstructed data.

2.2.2 Reconstruction of the data from fibroadenoma

The reconstructed data by the FPT$^{(-)}$ for the fibroadenoma are presented in Table 3, for $N_P = 1000$, $N_P = 1500$ and $N_P = 2000$. At $N_P = 1000$ (upper panel (i) of Table 3),

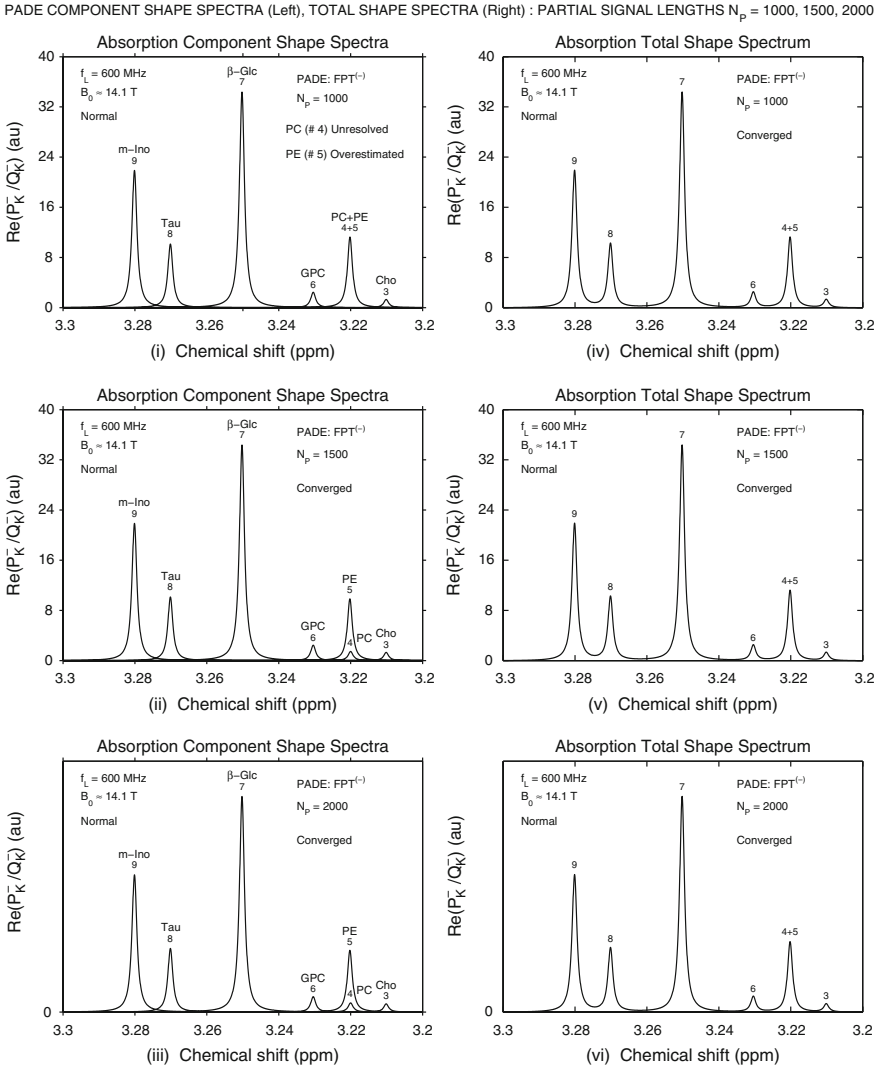

Fig. 1 Convergence patterns for the Padé-reconstructed the absorption component spectra (left panels) and total shape spectra (right panels) for normal breast within the frequency range of 3.2 to 3.3 ppm, from in vitro data of Ref. [55]. In the top right panel (iv), the total shape spectrum is converged at $N_P = 1000$, but the component spectrum at $N_P = 1000$ (top left panel (i)) failed to resolve phosphocholine (PC) (peak #4) and overestimated phosphoethanolamine (PE) (peak #5). At $N_P = 1500$ (middle left panel (ii)) the two resonances (## 4 & 5) at 3.22 ppm are resolved; the small PC peak is seen to completely underlie PE. Convergence of the absorption component spectra (iii) and total shape spectra (vi) remains stable at $N_P = 2000$ (bottom panels) and beyond including the full signal length N. The ordinates are in au

again only eight of the nine resonances were identified. In the interval where there should be two peaks, PC (peak #4) at 3.220012 ppm and PE (peak #5) at 3.220215 ppm, only one resonance was identified at 3.220169. Again, since this single peak was closer to PE, it was given that assignment. At $N_P = 1000$, the reconstructed amplitude and the concentration for that single resonance were approximately the sum of (PC + PE).

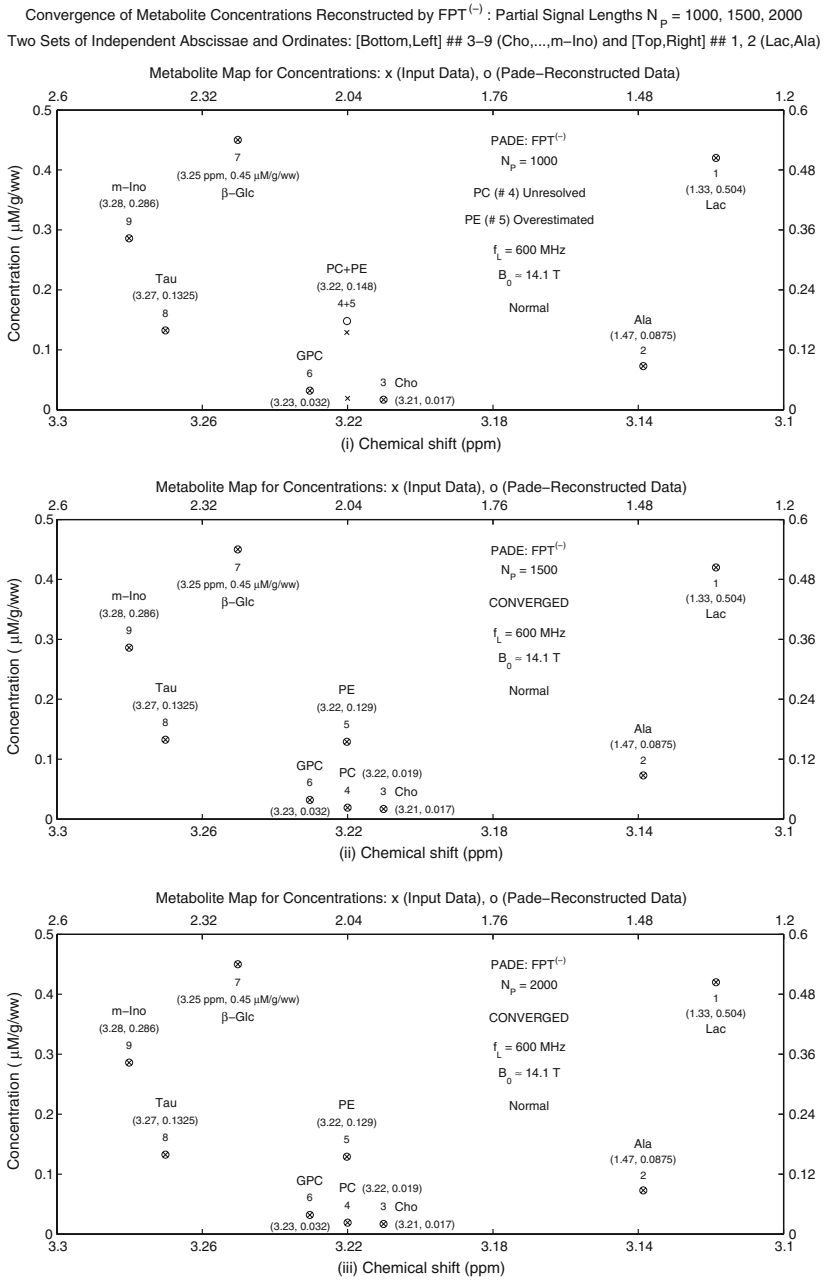

Fig. 2 Convergence of the Padé-reconstructed metabolite concentrations in normal breast from in vitro data of Ref. [55]. At $N_P = 1000$ (top panel (i)) convergence has not been achieved. PC (peak #4) is not detected and PE (peak #5) is overestimated. All of the other metabolite concentrations are fully correct at the 4^{th} decimal place. At $N_P = 1500$ (middle panel (ii)) all the resonances are identified and the reconstructed metabolite concentrations are correct. This convergence is stable at longer signal lengths, as shown in bottom panel (iii) at $N_P = 2000$ and beyond, including the full signal length N

At $N_P = 1000$ all the reconstructed spectral parameters were completely exact for Lac (peak #1), Ala (peak #2), β-Glc (peak #7), Tau (peak #8) and m-Ino (peak #9) . However, for Cho (peak #3) the chemical shift frequency, Re(f_k) and the line width, Im(f_k) were correct for five of the six digits (3.210122 ppm rather than 3.210124 ppm, 0.000830 ppm rather than 0.000833 ppm, respectively). The reconstructed amplitude $|d_k|$ for Cho was fully correct, but the metabolite concentration was calculated to be 0.0219 µM/g/ww, rather than the correct value of 0.0220 µM/g/ww. For GPC (peak #6) the chemical shift frequency, Re(f_k) and the line width, Im(f_k) were correct for five of the six digits (3.230413 ppm rather than 3.230412 ppm, 0.000831 ppm rather than 0.000833 ppm, respectively). The reconstructed amplitude $|d_k|$ for GPC was fully correct, but the metabolite concentration was calculated to be 0.0689 µM/g/ww, rather than the correct value of 0.0690 µM/g/ww.

At $N_P = 1500$ full convergence was attained for all the reconstructed parameters for all nine resonances (middle panel (ii) of Table 3). The stability of convergence at higher signal length $N_P = 2000$ is demonstrated on the bottom panel (iii) of Table 3, in which it is seen that all the reconstructed parameters remain exact. This stable convergence was also confirmed at even longer signal lengths, including the full signal length N.

Figure 3 displays the absorption component shape spectra and the total shape spectra reconstructed by the FPT$^{(-)}$ at $N_P = 1000$, $N_P = 1500$ and $N_P = 2000$ for the fibroadenoma. At $N_P = 1000$, as seen on the right upper panel (iv), the absorption total shape spectrum is converged. Again, this was not the case for the component shape spectrum (left upper panel (i)), which shows only one peak (#5, PE) at 3.22 which is overestimated, while peak #4 (PC) is unresolved. At $N_P = 1500$ in the left middle panel (ii) of Fig. 3 the component shape spectrum is converged such that peaks ## 4 and 5 are resolved and have the correct heights, as do all the other peaks. The small PC peak is seen to be completely beneath PE. Stability of convergence is confirmed here as well at $N_P = 2000$ in the lower panels for both the absorption component shape spectrum (iii) and the total shape spectrum (vi) and this also holds true for longer signals lengths, including the full signal length N.

The convergence of metabolite concentrations for the fibroadenoma data at $N_P = 1000$, $N_P = 1500$ and $N_P = 2000$ is shown in Fig. 4. At $N_P = 1000$ neither the concentrations of PC nor PE are correctly assessed in the reconstruction (top panel (i)), and there is a slight discrepancy in the concentrations of peaks ## 3 and 6, Cho and GPC, respectively. At $N_P = 1500$ (middle panel (ii)) and $N_P = 2000$ (bottom panel (iii)), all of the metabolite concentrations are correct, as seen both numerically and by the graphic representations. At even higher N_P and and at the full signal length N the metabolite concentrations were verified to be correct, as well.

2.2.3 Reconstruction of the data from malignant breast

The reconstructed data by the FPT$^{(-)}$ for the malignant breast are presented in Table 4 at $N_P = 1000$, $N_P = 1500$ and $N_P = 2000$. At $N_P = 1000$ (upper panel (i) of Table 4), once again only eight of the nine resonances were identified. In the interval where there should be two peaks, PC at 3.220012 ppm and PE at 3.220215, there was only one resonance identified at 3.220166 ppm, and the reconstructed amplitudes and

Table 3 Padé-reconstructed spectral parameters and metabolite concentrations for fibroadenoma with the input data as derived from Ref. [55]

CONVERGENCE of SPECTRAL PARAMETERS and CONCENTRATIONS in FPT$^{(-)}$: PARTIAL SIGNAL LENGTHS N_P =1000, 1500, 2000

(i) Pade–Reconstructed Data (Fibroadenoma): N_P = 1000 (# 4 PC: Unresolved, # 5 PE: Overestimated)

N_k (Metabolite # k)	Re(f_k) (ppm)	Im(f_k) (ppm)	$\|d_k\|$ (au)	C_k (μM/g/ww)	M_k (Assignment)
1	1.330413	0.000832	0.05928	1.4820	Lac
2	1.470313	0.000834	0.00440	0.1100	Ala
3	3.210122	0.000830	0.00088	0.0219	Cho
5	3.220169	0.000835	0.01909	0.4773	PE
6	3.230413	0.000831	0.00276	0.0689	GPC
7	3.250224	0.000832	0.03912	0.9780	β–Glc
8	3.270141	0.000834	0.01352	0.3380	Tau
9	3.280132	0.000831	0.01860	0.4650	m–Ino

(ii) Pade–Reconstructed Data (Fibroadenoma): N_P = 1500 (Converged)

N_k (Metabolite # k)	Re(f_k) (ppm)	Im(f_k) (ppm)	$\|d_k\|$ (au)	C_k (μM/g/ww)	M_k (Assignment)
1	1.330413	0.000832	0.05928	1.4820	Lac
2	1.470313	0.000834	0.00440	0.1100	Ala
3	3.210124	0.000833	0.00088	0.0220	Cho
4	3.220012	0.000832	0.00432	0.1080	PC
5	3.220215	0.000831	0.01476	0.3690	PE
6	3.230412	0.000833	0.00276	0.0690	GPC
7	3.250224	0.000832	0.03912	0.9780	β–Glc
8	3.270141	0.000834	0.01352	0.3380	Tau
9	3.280132	0.000831	0.01860	0.4650	m–Ino

(iii) Pade–Reconstructed Data (Fibroadenoma): N_P = 2000 (Converged)

N_k (Metabolite # k)	Re(f_k) (ppm)	Im(f_k) (ppm)	$\|d_k\|$ (au)	C_k (μM/g/ww)	M_k (Assignment)
1	1.330413	0.000832	0.05928	1.4820	Lac
2	1.470313	0.000834	0.00440	0.1100	Ala
3	3.210124	0.000833	0.00088	0.0220	Cho
4	3.220012	0.000832	0.00432	0.1080	PC
5	3.220215	0.000831	0.01476	0.3690	PE
6	3.230412	0.000833	0.00276	0.0690	GPC
7	3.250224	0.000832	0.03912	0.9780	β–Glc
8	3.270141	0.000834	0.01352	0.3380	Tau
9	3.280132	0.000831	0.01860	0.4650	m–Ino

the concentrations for that single resonance were approximately the sum of (PC + PE). Again, since this single peak was closer to PE, it was given that assignment. At $N_P = 1000$ all the reconstructed spectral parameters were completely exact for Lac (peak #1), Ala (peak #2) and m-Ino (peak #9). For peak #3 (Cho) the reconstructed Re(f_k) and Im(f_k) were exact to five of six decimal places (3.210122 ppm instead of the correct value of 3.210124 and 0.000830 ppm instead of the correct value of 0.000834 ppm, respectively). The reconstructed $|d_k|$ for choline was 0.00444 au whe-

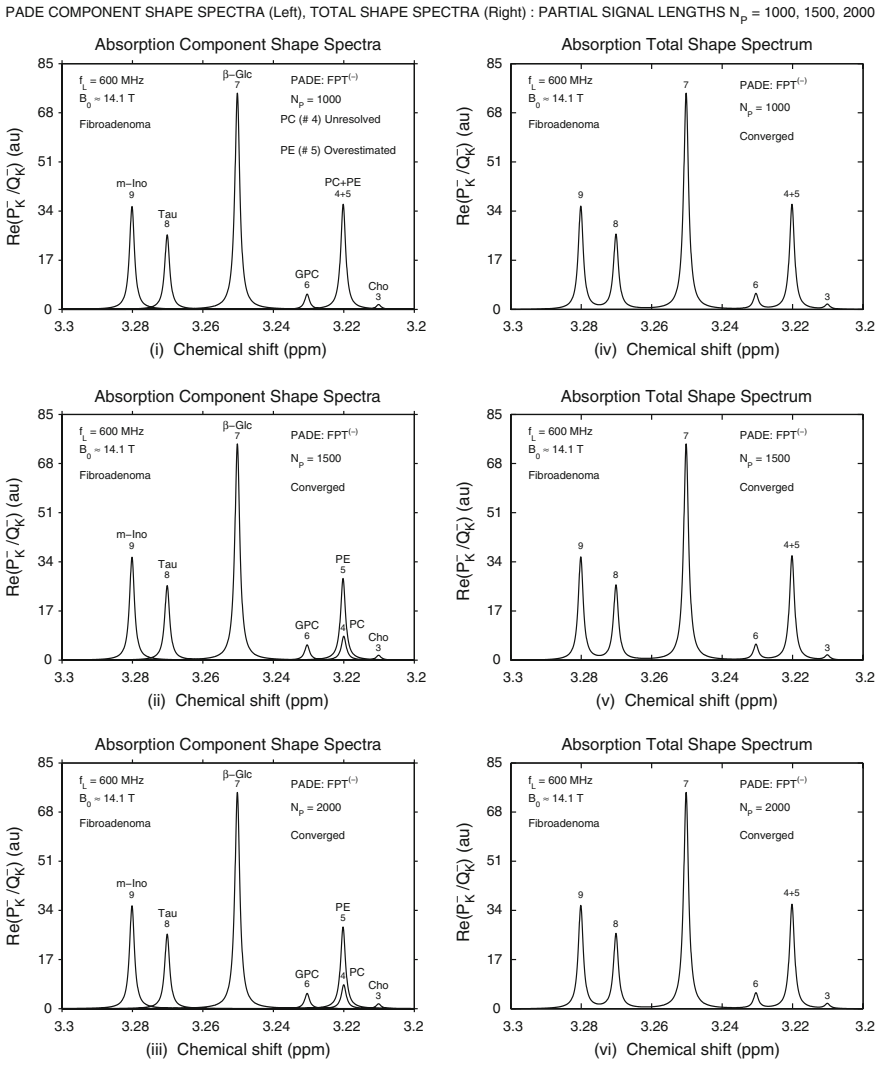

Fig. 3 Convergence patterns for the Padé-reconstructed the absorption component spectra (left panels) and total shape spectra (right panels) for fibroadenoma within the frequency range of 3.2 to 3.3 ppm, from in vitro data of Ref. [55]. In the top right panel (iv), the total shape spectrum is converged at $N_P = 1000$, but the component spectrum at $N_P = 1000$ (top left panel (i)) failed to resolve PC (peak #4) and overestimated PE (peak #5). At $N_P = 1500$ (middle left panel (ii)) the two resonances (## 4 & 5) at 3.22 ppm are resolved; PC is seen to completely underlie PE. At $N_P = 2000$ (bottom panels) convergence of the absorption component spectra (iii) and total shape spectra (vi) remains stable and this holds for longer signal lengths, as well, including the full signal length N. The ordinates are in au

reas the correct value is 0.00446 au. The concentration for choline was calculated to be 0.1111 μM/g/ww at $N_P = 1000$, while it should be 0.1115 μM/g/ww. For peak # 6 (GPC) at $N_P = 1000$ the reconstructed Re(f_k) was correct to five of six decimal places; the Im(f_k) to four of six decimal places, the $|d_k|$ was 0.00933 au rather than 0.00936, and the concentration was 0.2332 μM/g/ww while the correct value is

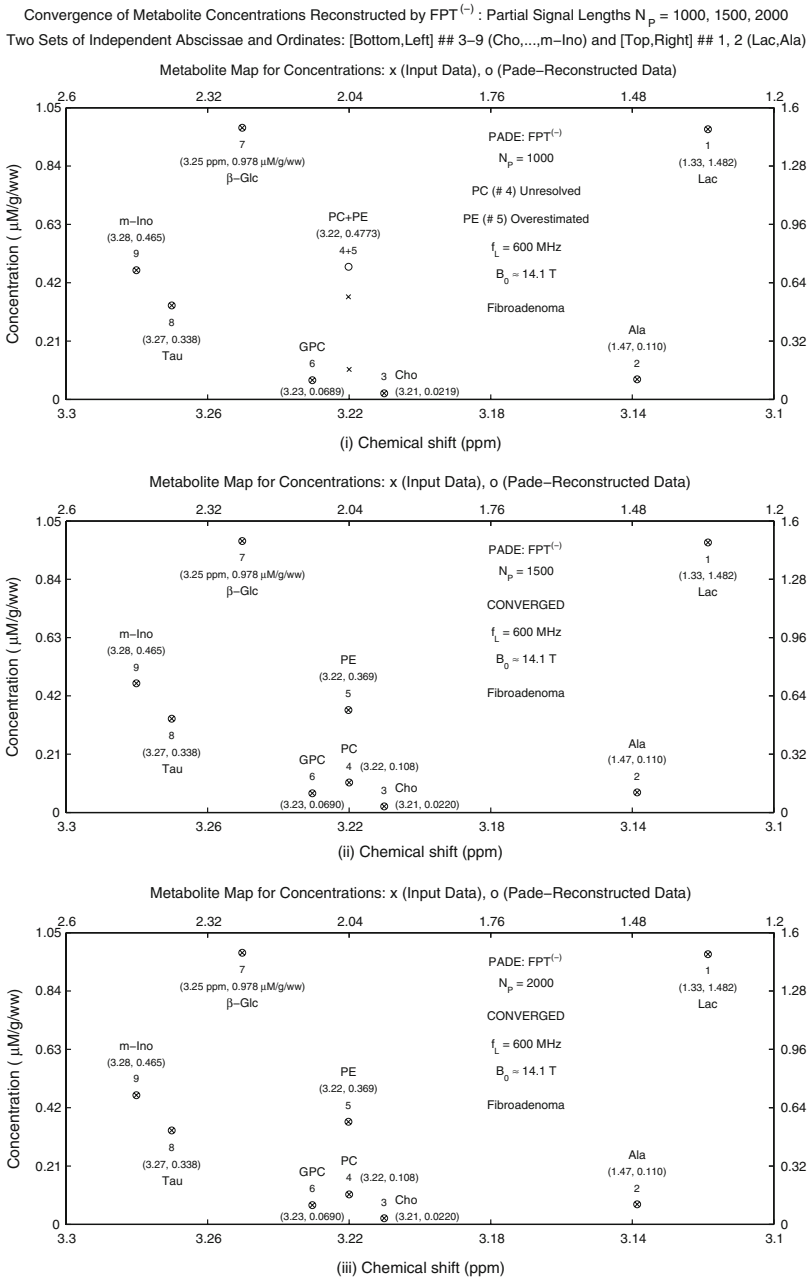

Fig. 4 Convergence of the Padé-reconstructed metabolite concentrations in fibroadenoma from in vitro data of Ref. [55]. At $N_P = 1000$ (top panel (i)) convergence has not been achieved. Peak #4 (PC) is not detected and peak #5 (PE) is overestimated. Peaks ## 3 (Cho) and 6 (GPC) were correct only to 2 decimal places. All of the other metabolite concentrations are fully correct at the 4^{th} decimal place. At $N_P = 1500$ (middle panel (ii)) all the resonances are identified and the reconstructed metabolite concentrations are correct. This convergence is stable as shown in bottom panel (iii) at $N_P = 2000$, and this holds for longer signal lengths, including the full signal length N

Table 4 Padé-reconstructed spectral parameters and metabolite concentrations for breast cancer from the input data as derived from Ref. [55]

CONVERGENCE of SPECTRAL PARAMETERS and CONCENTRATIONS in FPT$^{(-)}$: PARTIAL SIGNAL LENGTHS N_P =1000, 1500, 2000

(i) Pade–Reconstructed Data (Malignant): N_P = 1000 (# 4 PC: Unresolved, # 5 PE: Overestimated)

N_k (Metabolite # k)	Re(f_k) (ppm)	Im(f_k) (ppm)	$\|d_k\|$ (au)	C_k(μM/g/ww)	M_k (Assignment)
1	1.330413	0.000831	0.32474	8.1185	Lac
2	1.470313	0.000832	0.03156	0.7890	Ala
3	3.210122	0.000830	0.00444	0.1111	Cho
5	3.220166	0.000836	0.10230	2.5575	PE
6	3.230414	0.000829	0.00933	0.2332	GPC
7	3.250224	0.000832	0.02882	0.7204	β–Glc
8	3.270141	0.000831	0.11182	2.7954	Tau
9	3.280132	0.000833	0.03564	0.8910	m–Ino

(ii) Pade–Reconstructed Data (Malignant): N_P = 1500 (Converged)

N_k (Metabolite # k)	Re(f_k) (ppm)	Im(f_k) (ppm)	$\|d_k\|$ (au)	C_k(μM/g/ww)	M_k (Assignment)
1	1.330413	0.000831	0.32474	8.1185	Lac
2	1.470313	0.000832	0.03156	0.7890	Ala
3	3.210124	0.000834	0.00446	0.1115	Cho
4	3.220012	0.000831	0.02448	0.6120	PC
5	3.220215	0.000832	0.07776	1.9440	PE
6	3.230412	0.000833	0.00936	0.2340	GPC
7	3.250224	0.000832	0.02882	0.7205	β–Glc
8	3.270141	0.000831	0.11182	2.7955	Tau
9	3.280132	0.000833	0.03564	0.8910	m–Ino

(iii) Pade–Reconstructed Data (Malignant): N_P = 2000 (Converged)

N_k (Metabolite # k)	Re(f_k) (ppm)	Im(f_k) (ppm)	$\|d_k\|$ (au)	C_k(μM/g/ww)	M_k (Assignment)
1	1.330413	0.000831	0.32474	8.1185	Lac
2	1.470313	0.000832	0.03156	0.7890	Ala
3	3.210124	0.000834	0.00446	0.1115	Cho
4	3.220012	0.000831	0.02448	0.6120	PC
5	3.220215	0.000832	0.07776	1.9440	PE
6	3.230412	0.000833	0.00936	0.2340	GPC
7	3.250224	0.000832	0.02882	0.7205	β–Glc
8	3.270141	0.000831	0.11182	2.7955	Tau
9	3.280132	0.000833	0.03564	0.8910	m–Ino

0.2340 μM/g/ww. For peak #7 (β-Glc) and peak #8 (Tau), the reconstructed Re(f_k), Im(f_k) and $|d_k|$ were correct to all decimal places, but the calculated concentrations were exact to three of the four decimal places.

At $N_P = 1500$ full convergence was attained for all the reconstructed parameters for all nine resonances, middle panel (ii) of Table 4. Once again, the stability of convergence at higher signal lengths $N_P = 2000$ is demonstrated, where on the bot-

tom panel (iii) of Table 4, it is seen that all the reconstructed parameters remain exact. This remains true for even higher signal lengths, including the full signal length N.

The Padé-reconstructed absorption component shape spectra and the total shape spectra are shown in Fig. 5 at $N_P = 1000$, $N_P = 1500$ and $N_P = 2000$ for the malignant breast data. At $N_P = 1000$, (right upper panel (iv)), the absorption total shape spectrum is converged. Once again, this was not the case for the component shape spectrum (left upper panel (i)), which shows only one peak (#5, PE) at 3.22 which is overestimated, while peak #4 (PC) is unresolved. At $N_P = 1500$ in the left middle panel (ii) of Fig. 5 the component shape spectrum is converged such that peaks ## 4 and 5 are resolved and have the correct heights, as do all the other peaks. Phosphocholine is seen to lie completely underneath PE. Stability of convergence is confirmed at $N_P = 2000$ in the lower panels for both the absorption component shape spectrum (iii) and the total shape spectrum (vi), and this was the case for longer signal lengths, as well, including the full signal length N.

The convergence of metabolite concentrations for the breast cancer data is shown on Fig. 6 for $N_P = 1000$, $N_P = 1500$ and $N_P = 2000$. Prior to convergence, at $N_P = 1000$ neither the concentrations of peaks ## 4 (PC) nor 5 (PE) are correctly assessed in the reconstruction (top panel (i)) and there is a slight discrepancy in the concentrations of peak # 3 (Cho), peak # 6 (GPC), peak # 7 (β-Glc) and peak # 8 (Tau). At $N_P = 1500$ (middle panel (ii)) and $N_P = 2000$ (bottom panel (iii)), all of the metabolite concentrations are observed to be correct, both numerically and by the graphic representations. We verified that the metabolite concentrations were correct even for higher N_P and at the full signal length N.

2.2.4 Comparison of the converged spectra and concentration maps for normal breast, fibroadenoma and breast cancer

In Fig. 7 the converged Padé-reconstructed absorption component shape spectra and total shape spectra within the range of 3.2 to 3.3 ppm are shown for the normal breast data (top panels (i) and (iv)), fibroadenoma (middle panels (ii) and (v)) and malignant breast data (bottom panels (iii) and (vi)). For the normal data, the amplitudes of all the metabolites within this frequency range are low, with β-Glc at 3.25 ppm (peak #7) being the largest, followed by m-Ino (peak #9) at 3.28 ppm. The PC peak underlying PE is very small.

Compared to the spectra for the normal breast, for the fibroadenoma the amplitudes of all the peaks are larger within the range of 3.2 and 3.3 ppm. As is the case for the normal data, β-Glc at 3.25 ppm (peak #7) predominates in the spectrum of the fibroadenoma within this frequency range. The difference between the total absorption shape spectrum and the component spectrum becomes apparent for the fibroadenoma, since the peak (4+5) at 3.22 ppm is approximately the same height as m-Ino (peak #9 at 3.28 ppm) for the total shape spectrum, while m-Ino is clearly larger than the resolved peaks ## 4 (PC) and 5 (PE) at 3.22 ppm in the converged component shape spectrum.

The spectra for the breast cancer data show a clearly different pattern within the range of 3.2 and 3.3 ppm. Peak #8 (Tau) at 3.27 ppm is predominant for the malignant

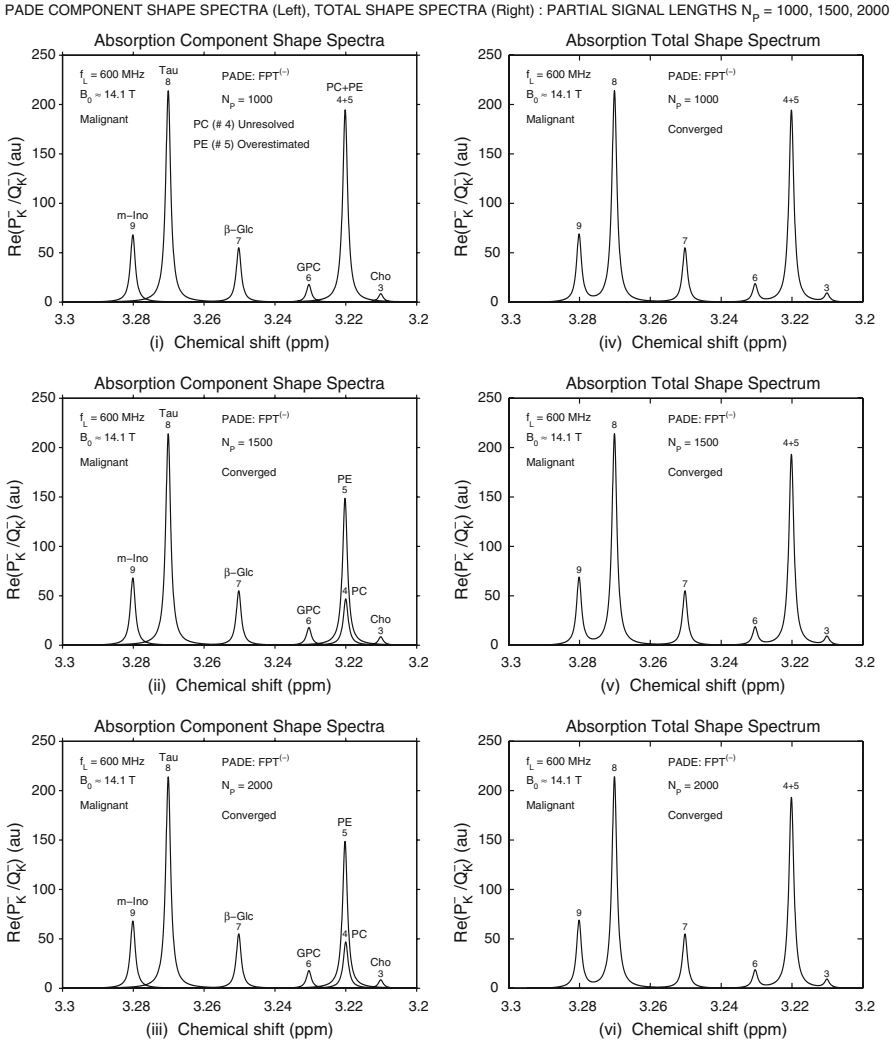

Fig. 5 Convergence patterns for the Padé-reconstructed the absorption component spectra (left panels) and total shape spectra (right panels) for breast cancer within the frequency range of 3.2 to 3.3 ppm, from in vitro data of Ref. [55]. In the top right panel (iv), the total shape spectrum is converged at $N_P = 1000$, but the component spectrum at $N_P = 1000$ (top left panel (i)) failed to resolve PC (peak #4) and overestimated PE (peak #5). At $N_P = 1500$ (middle left panel (ii)) the two resonances (##4 & 5) at 3.22 ppm are resolved; PC is seen to completely underlie PE. At $N_P = 2000$ (bottom panels) convergence of the absorption component spectra (iii) and total shape spectra (vi) remains stable, and this holds for longer signal lengths, as well. The ordinates are in au

case, with peak # 7 (β-Glc) at 3.25 ppm being among the smaller resonances. For the malignant data the difference is the most marked between the total shape spectrum in which the PC+PE peak at 3.22 is nearly as large as most abundant resonance, Tau, and the component spectrum in which PE and PC are clearly delineated and each obviously much smaller than Tau.

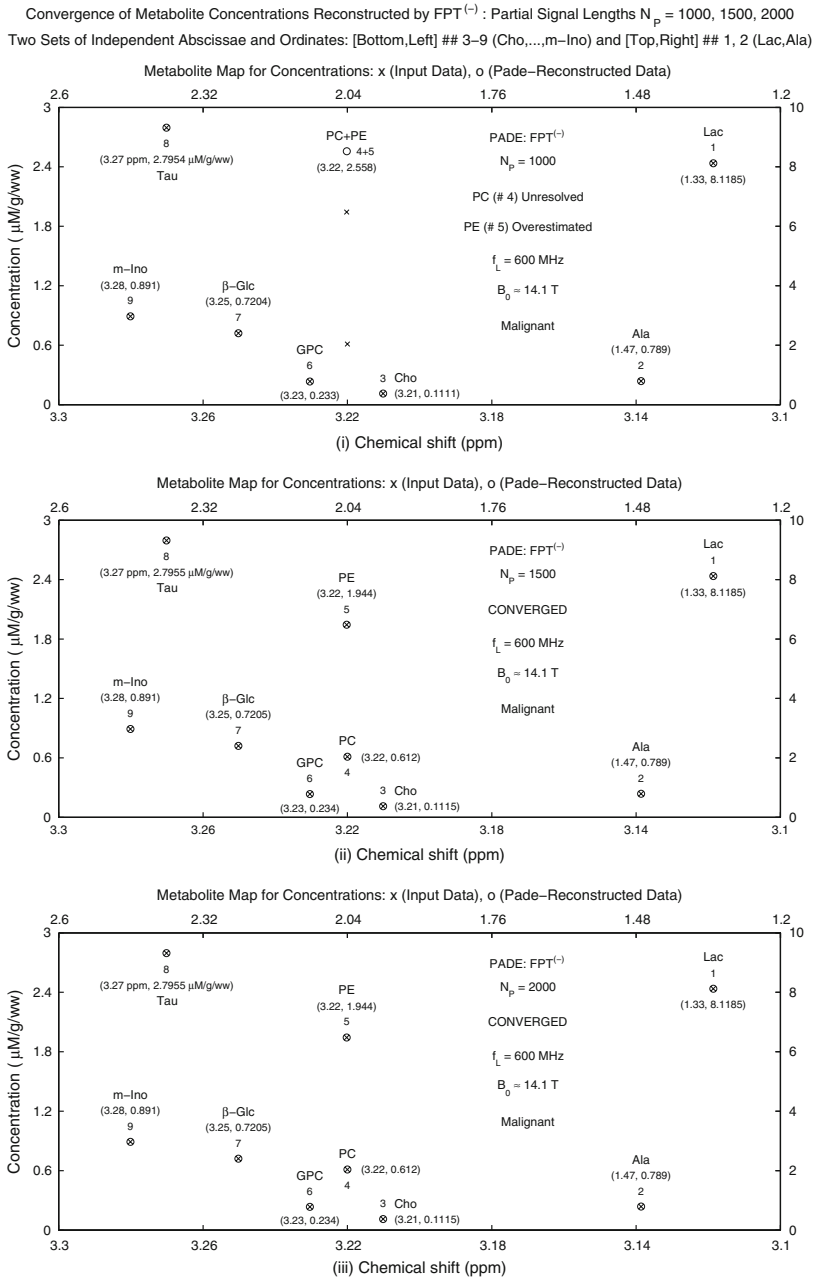

Fig. 6 Convergence of the Padé-reconstructed metabolite concentrations in breast cancer from in vitro data of Ref. [55]. At $N_P = 1000$ (top panel (i)) convergence has not been achieved. PC is not detected, PE is overestimated and several of the other metabolite concentrations are not fully correct at the 4th decimal place. At $N_P = 1500$ (middle panel (ii)) all the resonances are identified and the reconstructed metabolite concentrations are correct. This convergence is stable at $N_P = 2000$ as shown in bottom panel (iii), as well as at longer signal lengths, including the full signal length N

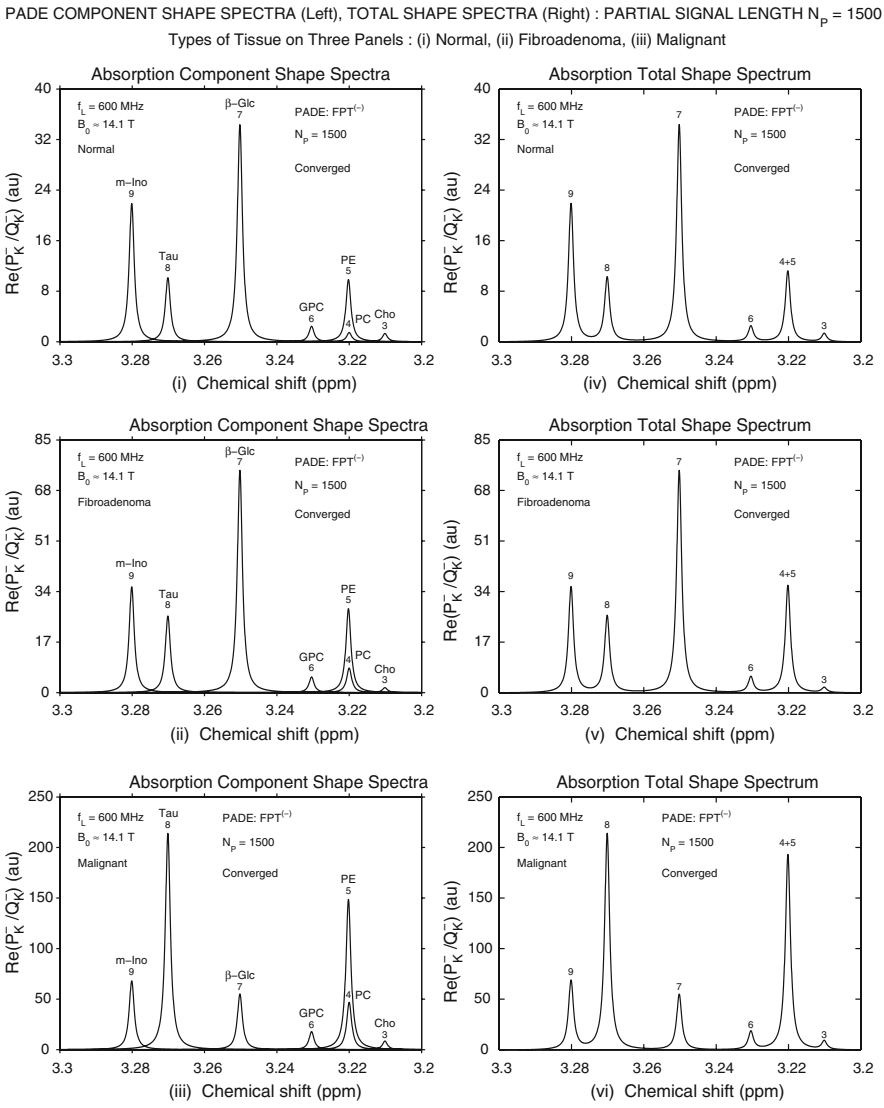

Fig. 7 Converged Padé-reconstructed absorption component spectra (left panels) and total shape spectra (right panels) at $N_P = 1500$ for normal breast tissue breast tissue (top panels (i and iv)), fibroadenoma (middle panels (ii and v) and malignant breast (bottom panels (iii) and (vi)) derived from in vitro data of Ref. [55]

The converged metabolite maps reconstructed by the FPT$^{(-)}$ for the normal breast tissue (top panel (i)), fibroadenoma (middle panel (ii)) and for the malignant breast (bottom panel (iii)) are presented in Fig. 8. For the normal breast tissue it can be seen that peak # 1 (Lac), has the largest concentration (0.5040 µM/g/ww), slightly higher than β-Glc, peak #7 (0.4500 µM/g/ww). The median lactate concentration in the normal breast is about 0.34 of that in the fibroadenoma. For the malignant breast,

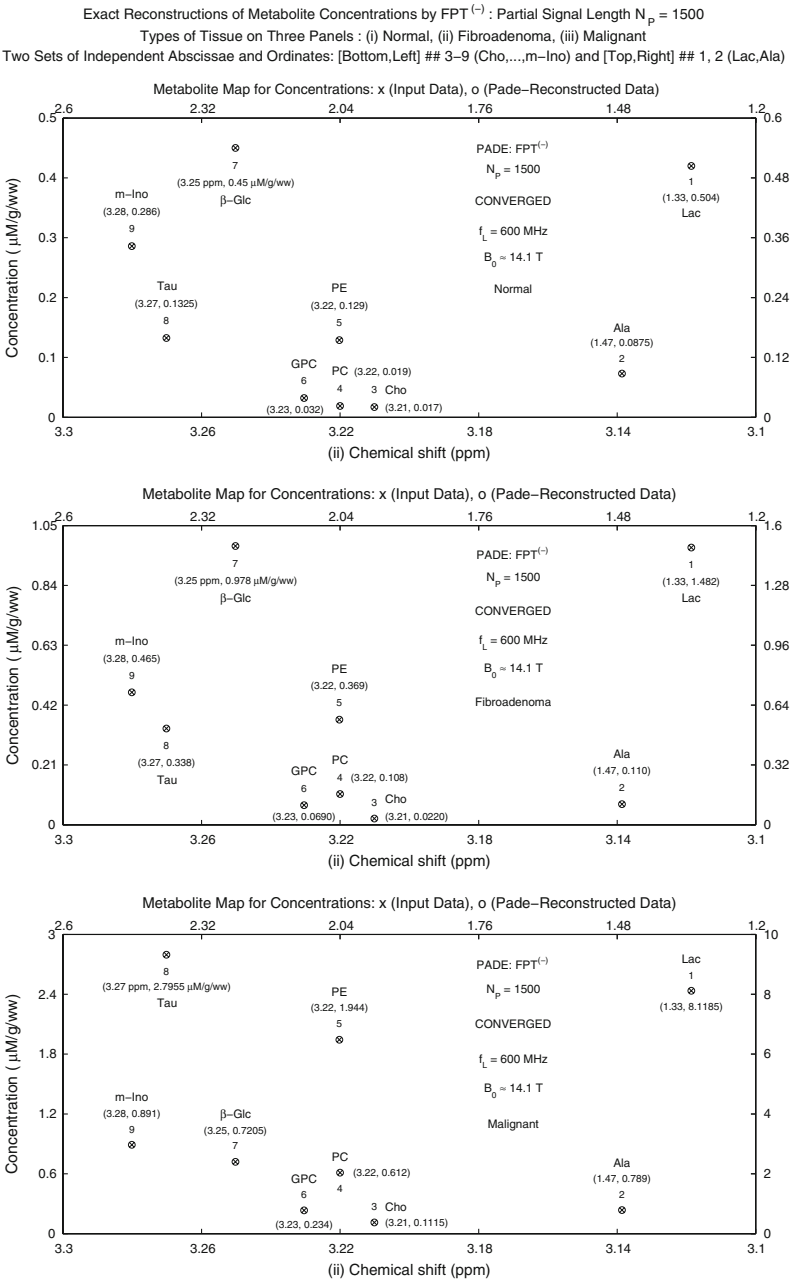

Fig. 8 Converged Padé-reconstructed metabolite concentrations $N_P = 1500$ for normal breast tissue breast tissue (top panel (i)), fibroadenoma (middle panel (ii) and malignant breast (bottom panel (iii)) derived from *in vitro* data of Ref. [55]

the lactate concentration is over five times higher than in the fibroadenoma, and is by far the largest resonance, being almost three time higher than Tau (peak #8).

3 Discussion

A key advantage of the FPT for MRS signals is the ability to resolve and precisely quantify very closely overlapping resonances with certainty. In the present study this is clearly demonstrated for the spectrally dense region between 3.21 and 3.23 ppm, which encompasses the constituents of total choline: choline at 3.21 ppm, phosphocholine at 3.22 ppm and glycerophosphocholine at 3.23 ppm. Remarkably, phosphocholine and phosphoethanolamine are almost completely overlapping at 3.22 ppm, separated by a mere 0.000203 ppm which is about four times less than the line widths. Yet at convergence the $\mathrm{FPT}^{(-)}$ exactly reconstructs the input parameters for these two resonances with full fidelity. In our previous work [12,14,17] from MRS time signals that closely match FIDs encoded via proton MRS from the brain of a healthy volunteer [59], the FPT at convergence also exactly reconstructed all the resonances (25 in that case) including two that were nearly degenerate.

The present study also corroborates our previous findings [12] that convergence of the total shape spectrum does not necessarily imply that the component spectrum has done likewise. Thus, the commonly employed practice of relying upon the residual spectrum to indicate convergence [59], is indeed tenuous at best, and, in fact, entails attempts to guess the number of resonances under a given peak, as customarily done by various post-processing fitting algorithms used in the MRS literature [60–62]. This is due to the reliance upon Fourier-based processing, which can only provide a total shape spectrum. In sharp contradistinction, Padé-based reconstruction, because of its fundamental grounding in quantum mechanics and through the powerful concept of pole-zero cancellation (Froissart doublets), yields not only the possibility of the exact extraction of all the spectral frequencies and amplitudes of all the metabolites, but also certainty about their true number. The key clinical ramification of this latter feature is the unique, and, hence, the most reliable quantification of all the physical metabolite concentrations [15].

Identification and quantification of these constituents of total choline within the tight spectral region of 3.21 to 3.23 ppm has clinical relevance for breast cancer diagnostics. We have previously noted that the ratio of PC/GPC is significantly higher in the malignant versus the normal samples [54] of the present input data [55]. This corroborates human breast cell line research, indicating that malignant transformation is associated with a so-called "glycerophosphocholine to phosphocholine switch" [63], related, *inter alia*, to over-expression of the enzyme choline kinase responsible for PC synthesis [64,65], and also reflecting altered membrane choline phospholipid metabolism. The major steps in choline metabolism are through the cytosine diphosphate (CDP)-choline pathway [65]. The ^{1}H-NMR visible compounds within that pathway, choline (3.21 ppm), PC (3.22 ppm) and GPC (3.23 ppm) underscore the clinico-biological importance of analyzing the relationship among these closely overlapping resonances. On the other hand, by summing these three metabolites as "total choline", as is currently done with in vivo MRS, substantial information for breast cancer diagnostics is missed.

Precise quantification of the metabolites within this tight spectral region may be of added value in distinguishing fibroadenoma from breast cancer. From the present input data [55], the PC concentration was approximately 5.7 times lower in the fibroadenoma than the median PC concentration for breast cancer. This was percentually a greater difference than for PE or GPC. On the other hand, the PC and GPC concentrations, in the fibroadenoma were respectively about 5.7 and 2.2 times higher than in the median PC concentration for normal breast tissue. These findings illustrate the need for precise quantification of the components of total choline in order to develop reliable databases to improve the diagnostic accuracy with which benign and malignant breast pathology are distinguished.

On the basis of these input data from a fairly small number of breast cancer samples and only one fibroadenoma, obviously no definitive conclusions can be drawn about which metabolites are optimal for detecting the presence of breast cancer and distinguishing this from normal mammary tissue or benign lesions. Nevertheless, it is noteworthy that we found in our multiple logistic regression analysis [40,53,54] of these data by Gribbestad et al. [55] that only lactate showed 100% diagnostic accuracy both with and without inclusion of the fibroadenoma. Thus, we see that the lactate concentration from the present input data based on Ref. [55] was lower in the fibroadenoma than in all the individual breast cancer samples.

Some corroboration about the diagnostic value of lactate and of phosphocholine is provided by Sharma and colleagues [67] who used in vitro 2D MRS to compare 11 involved and 12 uninvolved lymph nodes from patients with breast cancer. Namely, the concentrations of PC and GPC were significantly higher in involved compared to non-involved nodes. This was attributed to increased membrane synthesis in cancer cells, suggesting that metastatic breast cancer cells were present in the lymph nodes. There was also a highly significant difference between the lactate concentrations in involved and non-involved nodes [66]. The elevated lactate reflects the presence of cancer cells whose energy source is from the anaerobic glycolytic pathway. Animal models of breast cancer also support the importance of assessing the rate of glycolysis and lactate clearance with respect to the diagnosis and prognosis of breast cancer [67]. Thus far, however, clinical in vivo MRS analyses have not included lactate as a metabolic marker of breast cancer.

The present study employs noise-free FIDs, since we wanted to set up the fully-controlled standard for the FPT in the case of the initial application of this method to data within the realm of breast cancer diagnostics by MRS. This is methodologically justified [12]. We are now taking the next steps to extend our analysis to both noise-corrupted synthesized data (still well-controlled) and to encoded FIDs similar to those from Ref. [55] as well as in vivo MRS data from the breast, and these results will be reported shortly.

4 Conclusions

The advantages of the FPT demonstrated in the present paper could be of definite benefit for breast cancer diagnostics via MRS. This line of investigation should continue with encoded data from benign and malignant breast tissue, in vitro and in vivo. We

anticipate that Padé-optimized MRS will reduce the false positive rates of MR-based modalities and further improve their sensitivity. Once this is achieved, and given that MR entails no ionizing radiation, new possibilities for screening/early detection open up, especially for risk groups, e.g. Padé-optimized MRS could be used with greater surveillance frequency among younger women with high breast cancer risk.

Acknowledgements This work has been supported by King Gustav the 5th Jubilee Foundation, the Signe and Olof Wallenius Foundation and the Karolinska Institute Research Fund.

References

1. Dž. Belkić, K. Belkić, Decisive role of mathematical methods in early cancer diagnostics. J. Math. Chem. **42**, 1 (2007)
2. S. Hankinson, D. Hunter, in *Breast Cancer*, ed. by H.-O. Adami, D. Hunter, D. Trichopoulos. Textbook of Cancer Epidemiology (Oxford University Press, Oxford, 2002), pp. 301–339
3. S. Masood, Coming together to conquer the fight against breast cancer in countries of limited resources: the challenges and the opportunities. Breast J. **13**, 223 (2007)
4. D.M. Parkin, L.M. Fernandez, Use of statistics to assess the global burden of breast cancer. Breast J. **12**(Suppl 1), S70 (2006)
5. Dž. Belkić, P.A. Dando, J. Main, H.S. Taylor, Three novel high-resolution nonlinear methods for fast signal processing. J. Chem. Phys. **113**, 6542 (2000)
6. Dž. Belkić, Fast Padé Transform (FPT) for magnetic resonance imaging and computerized tomography. Nucl. Instrum. Methods Phys. Res. A **471**, 165 (2001)
7. Dž. Belkić, Strikingly stable convergence of the fast Padé transform (FPT) for high-resolution parametric and non-parametric signal processing of Lorentzian and non-Lorentzian spectra. Nucl. Instrum. Methods. Phys. Res. A **525**, 366 (2004)
8. Dž. Belkić, Error analysis through residual frequency spectra in the fast Padé transform (FPT). Nucl. Instrum. Methods Phys. Res. A **525**, 379 (2004)
9. Dž. Belkić, Analytical continuation by numerical means in spectral analysis using the fast Padé transform (FPT). Nucl. Instrum. Methods Phys. Res. A **525**, 372 (2004)
10. Dž. Belkić, *Quantum Mechanical Signal Processing and Spectral Analysis* (Institute of Physics Publishing, Bristol, 2005)
11. Dž. Belkić, K. Belkić, The fast Padé transform in magnetic resonance spectroscopy for potential improvements in early cancer diagnostics. Phys. Med. Biol. **50**, 4385 (2005)
12. Dž. Belkić, Exact quantification of time signals in Padé-based magnetic resonance spectroscopy. Phys. Med. Biol. **51**, 2633 (2006)
13. Dž. Belkić, Exponential convergence rate (the spectral convergence) of the fast Padé transform for exact quantification in magnetic resonance spectroscopy. Phys. Med. Biol. **51**, 6483 (2006)
14. Dž. Belkić, K. Belkić, The general concept of signal-noise separation (SNS): mathematical aspects and implementation in magnetic resonance spectroscopy. J. Math. Chem. (2008) doi:10.1007/s10910-007-9344-5
15. Dž. Belkić, K. Belkić, Unequivocal disentangling genuine from spurious information in time signals: clinical relevance in cancer diagnostics through magnetic resonance spectroscopy. J. Math. Chem. (2008) doi:10.1007/s10910-007-9337-4.
16. Dž. Belkić, K. Belkić, In vivo magnetic resonance spectroscopy by the fast Padé transform. Phys. Med. Biol. **51**, 1049 (2006)
17. Dž. Belkić, Machine accurate quantification in magnetic resonance spectroscopy. Nucl. Instrum. Methods Phys. Res. A **580**, 1034 (2007)
18. Dž. Belkić, Strikingly stable convergence of the fast Padé transform. J. Comp. Methods Sci. Eng. **3**, 299 (2003)
19. Dž. Belkić, Padé-based magnetic resonance spectroscopy (MRS). J. Comp. Methods Sci. Eng. **3**, 563 (2003)
20. W.W.F. Pijnappel, A. van den Boogaart, R. de Beer, D. van Ormondt, SVD-based quantification of magnetic resonance signals. J. Magn. Reson. **97**, 122 (1992)

21. M. Froissart, *Approximation de Padé: application à la Physique des Particules Élémentaires, CNRS, RCP, Programme No. 25*, vol. 9 (CNRS, Strasburg, 1969), p. 1
22. K. Belkić, Resolution performance of the fast Padé transform: potential advantages for magnetic resonance spectroscopy in ovarian cancer diagnostics. Nucl. Instrum. Methods Phys. Res. A **580**, 874 (2007)
23. Dž. Belkić, K. Belkić, Mathematical modeling of an NMR chemistry problem in ovarian cancer diagnostics. J. Math. Chem. **43**, 395 (2008)
24. D. Saslow, C. Boetes, W. Burke, S. Harms, M.O. Leach, C.D. Lehman, et al. American Cancer Society Breast Cancer Advisory Group. American Cancer Society guidelines for breast screening with MRI as an adjunct to mammography. CA Cancer J. Clin. **57**, 75–89 (2007)
25. D.M. Parkin, F. Bray, P. Pisani, Global cancer statistics. CA Cancer J. Clin. **55**, 74–108 (2005)
26. K. Armstrong, E. Moye, S. Williams, J.A. Berlin, E.E. Reynolds, Screening mammography in women 40 to 49 years of age: a systematic review for the American College of Physicians. Ann. Intern. Med. **146**, 516–526 (2007)
27. W.A. Berg, J.D. Blume, J.B. Cormack, E.B. Mendelson, D. Lehrer, M. Bohm-Velez Pisan, et al. ACRIN 6666 Investigators. Combined screening with ultrasound and mammography vs mammography alone in women at elevated risk of breast cancer. JAMA **299**, 2151–2163 (2008)
28. N. Perry, M. Broeders, C. de Wolf, S. Törnberg, R. Holland, L. von Karsa, European guidelines for quality assurance in breast cancer screening and diagnosis. Fourth edition—summary document. Ann. Oncol. **19**, 614–622 (2008)
29. H. Kuni, I. Schmitz-Feuerhake, H. Dieckmann, Mammography screening—neglected aspects of radiation risks. Gesundheitswesen **65**, 44 (2003)
30. M.P. Laderoute, Improved safety and effectiveness of imaging predicted for MR mammography. Br. J. Cancer **90**, 278 (2004)
31. S. Schrading, C.K. Kuhl, Mammographic, US, and MR imaging phenotypes of familial breast cancer. Radiology **246**, 58 (2008)
32. M. Kriege, C.T. Brekelmans, H. Peterse, I.M. Obdeijn, C. Boetes, H.M. Zonderland, et al. Tumor characteristics and detection method in the MRISC screening program for the early detection of hereditary breast cancer. Breast Cancer Res. Treat. **102**, 357–363 (2007)
33. N. Houssami, R. Wilson, Should women at high risk of breast cancer have screening magnetic resonance imaging (MRI)? J. Breast **16**, 2 (2007)
34. S.J. Nass, C. Henderson, J.C. Lashof, (eds.) *Mammography and Beyond: Developing Technologies for the Early Detection of Breast Cancers* (National Academy Press, Washington, DC, 2001)
35. E.A. Morris, Breast cancer imaging with MRI. Radiol. Clin. N. Am. **40**, 443 (2002)
36. J. Yu, A. Park, E. Morris, L. Liberman, P.I. Borgen, T.A. King, MRI screening in a clinic population with a family history of breast cancer. Ann. Surg. Oncol. **15**, 452 (2008)
37. A. Iglesias, M. Arias, P. Santiago, M. Rodríguez, J. Mañas, C. Saborido, Benign breast lesions that simulate malignancy: magnetic resonance imaging with radiologic-pathologic correlation. Curr. Probl. Diagn. Radiol. **36**, 66 (2007)
38. M.L. Essink-Bot. A.J. Rijnsburger, S. van Dooren, H.J. de Koning, C. Seynaeve, Women's acceptance of MRI in breast cancer surveillance because of a familial or genetic predisposition. Breast **15**, 673 (2006)
39. M. Robson, Breast cancer surveillance in women with hereditary risk due to BRCA1 or BRCA2 mutations. Clin. Breast Cancer **5**, 260 (2004)
40. K. Belkić, Current dilemmas and future perspectives for breast cancer screening with a focus on optimization of magnetic resonance spectroscopic imaging by advances in signal processing. Isr. Med. Assoc. J. **6**, 610–618 (2004)
41. R. Katz-Brull, P.T. Lavin, R.E. Lenkinski, Clinical utility of proton magnetic resonance spectroscopy in characterizing breast lesions. J. Natl. Cancer Inst. **9**, 1197 (2002)
42. L. Bartella, E.A. Morris, D.D. Dershaw, L. Liberman, S.B. Thakur, C. Moskowitz, J. Guido, W. Huang, Proton MR spectroscopy with choline peak as malignancy marker improves positive predictive value for breast cancer diagnosis: preliminary study. Radiology **239**, 686–692 (2006)
43. L. Bartella, S.B. Thakur, E.A. Morris, D.D. Dershaw, W. Huang, E. Chough, M.C. Cruz, L. Liberman, Enhancing nonmass lesions in the breast: evaluation with proton (1H) MR spectroscopy. Radiology **245**, 80–87 (2007)
44. L. Bartella, W. Huang, Proton (1H) MR spectroscopy of the breast. Radiographics **27**(Suppl 1), S241 (2007)

45. S. Meisamy, P.J. Bolan, E.H. Baker, C.T. Le, F. Kelcz, M.C. Lechner, B.A. Luikens, R.A. Carlson, K.R. Brandt, K.K. Amrami, et al. Adding in vivo quantitative 1H MR spectroscopy to improve diagnostic accuracy of breast MR imaging: preliminary results of observer performance study at 4.0T. Radiology **236**, 465 (2005)
46. F. Sardanelli, A. Fausto, F. Podo, MR spectroscopy of the breast. Radiol. Med. (Torino) **113**, 56 (2008)
47. G.M. Tse, D.K. Yeung, A.D. King, H.S. Cheung, W.T. Yang, In vivo proton magnetic resonance spectroscopy of breast lesions: an update. Breast Cancer Res. Treat. **104**, 249 (2007)
48. L. Kwock, J.K. Smith, M. Castillo, M.G. Ewend, F. Collichio, D.E. Morris, T.W. Bouldin, S. Cush, Clinical role of proton magnetic resonance spectroscopy in oncology: brain, breast and prostate cancer. Lancet Oncol. **7**, 859 (2006)
49. J. Hu, Y. Yu, Z. Kou, W. Huang, Q. Jiang, Y. Xuan, T. Li, V. Sehgal, C. Blake, E.M. Haacke, R.L. Soulen, A high spatial resolution 1H magnetic resonance spectroscopic imaging technique for breast cancer with a short echo time. Magn. Reson. Imaging **26**, 360 (2008)
50. P. Stanwell, C. Mountford, In vivo proton MR spectroscopy of the breast. Radiographics **27**(Suppl 1), S253 (2007)
51. M. Tozaki, Proton MR spectroscopy of the breast. Breast Cancer **15**, 218 (2008)
52. L. Gluch, Magnetic resonance in surgical oncology. ANZ. J. Surg. **75**, 464 (2005)
53. K. Belkić, MR spectroscopic imaging in breast cancer detection: possibilities beyond the conventional theoretical framework for data analysis. Nucl. Instrum. Methods Phys. Res. A. **525**, 313 (2004)
54. Dž. Belkić, K. Belkić, Mathematical optimization of in vivo NMR chemistry through the fast Padé transform: potential relevance for early breast cancer detection by magnetic resonance spectroscopy. J. Math. Chem. **40**, 85 (2006)
55. I.S. Gribbestad, B. Sitter, S. Lundgren, J. Krane, D Axelson, Metabolite composition in breast tumors examined by proton nuclear magnetic resonance spectroscopy. Anticancer Res. **19**, 1737 (1999)
56. M.A. Jacobs, P.B. Barker, P.A. Bottomley, Z. Bhujwalla, D.A. Bluemke, Proton magnetic resonance spectroscopic imaging of human breast cancer: a preliminary study. J. Magn. Reson. Imaging **19**, 68 (2004)
57. J. Evelhoch, M. Garwood, D. Vigneron, M. Knopp, D. Sullivan, A. Menkens, et al. Expanding the use of magnetic resonance in the assessment of tumor response to therapy. Cancer Res. **65**, 7041 (2005)
58. J. Frahm, H. Bruhn, M.L. Gyngell, K.D. Merboldt, W. Hanicke, R. Sauter, Localized high-resolution proton NMR spectroscopy using stimulated echoes: initial applications to human brain in vivo. Magn. Reson. Med. **9**, 79 (1989)
59. M.G. Swanson, A.S. Zektzer, Z.L.Tabatabai, J. Simko, S. Jarso, K.R. Keshari, L. Schmitt, P.R. Carroll, K. Shinohara, D.B. Vigneron, J. Kurhanewicz, Quantitative analysis of prostate metabolites using 1H HR-MAS spectroscopy. Magn. Reson. Med. **55**, 1257 (2006)
60. J.W. van der Veen, R. de Beer, P.R. Luyten, D. van Ormondt, Accurate quantification of in vivo 31P NMR signals using the variable projection method and prior knowledge. Magn. Reson. Med. **6**, 92 (1988)
61. L. Vanhamme, A. van den Boogaart, S. van Haffel, Improved method for accurate and efficient quantification of MRS data with use of prior knowledge. J. Magn. Reson. **29**, 35 (1997)
62. S.W. Provencher, Estimation of metabolite concentrations from localized in vivo proton NMR spectra. Magn. Reson. Med. **30**, 672 (1993)
63. E.O. Aboagye, Z.M. Bhujwalla, Malignant transformation alters membrane choline phospholipid metabolism of human mammary epithelial cells. Cancer Res. **59**, 80 (1999)
64. R. Katz-Brull, D. Seger, D. Rivenson-Segal, E. Rushkin, H. Degani, Metabolic markers of breast cancer: enhanced choline metabolism and reduced choline-ether-phospholipid synthesis. Cancer Res. **62**, 1966 (2002)
65. K. Glunde, C. Jie, Z.M. Bhujwalla, Molecular causes of the aberrant choline phospholipid metabolism in breast cancer. Cancer Res. **64**, 4270 (2004)
66. U. Sharma, A. Mehta, V. Seenu, N.R. Jagannathan, Biochemical characterization of metastatic lymph nodes of breast cancer patients by in vitro 1H magnetic resonance spectroscopy: a pilot study. Magn. Reson. Imaging **22**, 697 (2004)
67. D. Rivenzon-Segal, R. Margalit, H. Degani, Glycolysis as a metabolic marker in orthotopic breast cancer, monitored by in vivo 13C MRS. Am. J. Physiol. Endocrinol. Metab. **283**, E623 (2002)